RESEARCH PAPER

Phytochemical-Mediated Green Synthesis of Fe_3O_4/γ-Fe_2O_3 Core–Corona Nanoparticles Using Prosopis cineraria Extract: Enhanced Antioxidant Synergy and Pharmaceutical Potential

Abdul Majeed Ansari[1], Dinesh[2], and Dr K. M. Sharma[3*]

[1]Research Scholar, Department of Chemistry, Career Point University, Kota, Rajasthan, India-324005
[2]Assistant Professor, Department of Chemistry, Swami Keshvanand Institute of Technology, Management & Gramothan-Jaipur, India-302017
[3]Professor, Department of Chemistry, Career Point University, Kota, Rajasthan, India-324005

ABSTRACT

Iron oxide nanoparticles (FeONPs) are the new promising bifunctional nanoparticles in nanopharmaceutical applications, but traditional preparations usually have poor colloidal stability and Fenton-mediated pro-oxidant activity. In this work, a corecorona nanoarchitecture of Fe_3O_4/γ-Fe_2O_3 was prepared by using a single-pot, phytochemical-mediated bioreduction of FeCl3.6H2O using aqueous extract of the xerophytic tree Prosopis cineraria, rich in quercetin, kaempferol, gallic acid and chlorogenic acid. The polyphenol-flavonoid corona doubled up as a reductant and electrosteric stabilizer. UV-Vis spectroscopy showed characteristic bands at 247, 380, 426 and 474nm and FTIR confirmed a bidentate Fe-carboxylate and catecholate chelation ($\Delta\nu \approx 265$ cm^{-1}). XRD analysis confirmed an inverse-spinel structure with a phase-pure inverse-spinel structure, a Scherrer crystallite size of 12.8 ± 1.1 nm, and surface charge -25.3 mV, which is consistent with electrosteric colloidal stability. The phytochemical-capped FeONPs exhibited a strong antioxidant synergy with respect to the free extract, which was 1.43-, 1.36- and 1.35-fold decreases in IC50 against DPPH (41.2 ± 1.3 μg mL^{-1}), ABTS (40.3 ± 1.5 μg mL^{-1}) and nitric oxide radicals (47.5 ± 1.8 μg mL^{-1}), respectively. Mechanistically, the corecorona interface reduces the bond-dissociation energy of phenolic OH groups, facilitates Fe^{2+}/Fe^{3+}-mediated regeneration of phenoxyl radicals, and suppresses Fenton-driven hydroxyl radical generation. These properties place the system in a green-synthesized, phytochemical-capped nanoplatform with a high potential of nutraceutical antioxidant formulations, magnetic drug delivery, and photo-responsive pharmaceutical applications.

Keywords: green synthesis; iron oxide nanoparticles; core–corona architecture; antioxidant synergy; Prosopis cineraria; nutraceuticals; nanopharmaceutics; magnetic drug delivery; phytochemical capping; oxidative stress

How to cite this article: Ansari AM, Dinesh, Sharma KM. Phytochemical-Mediated Green Synthesis of Fe_3O_4/γ-Fe_2O_3 Core–Corona Nanoparticles Using Prosopis cineraria Extract: Enhanced Antioxidant Synergy and Pharmaceutical Potential. Int J Drug Deliv Technol. 2026;16(5): 1111-1120. DOI: 10.25258/ijddt.16.5.104

1. INTRODUCTION

Oxidative stress, the imbalance between the production of reactive oxygen species (ROS) and the inherent antioxidant responses is the central pathophysiological driver in cardiovascular disease, neurodegeneration, diabetes mellitus, hepatic injury and carcinogenesis. Combination of high radical-scavenging potency and controlled biodistribution in pharmacological interventions is therefore highly desirable in nutraceutical and therapeutic applications. Within this context, Iron oxide nanoparticles hold a unique place in the functional nanomaterials landscape. It is by virtue of their tunable redox chemistry, surface-area-amplified reactivity, and the structural flexibility of the Fe_3O_4/γ-Fe_2O_3 spinel system (Ali, R. 2025). Notably, FeONPs already have regulatory precedence in nanomedicine: ferumoxytol, ferucarbotran and other superparamagnetic iron oxide preparations are both clinically approved for iron-replacement therapy and use as contrast agents in magnetic resonance imaging (Anselmo and Mitragotri, 2019; Dadfar et al., 2019).

The integration of plant-derived reductants in the synthesis of these materials has emerged as a sustainable route to bifunctional nanohybrids. It provides with an inorganic core and an organic corona that co-operates to deliver amplified electron-transfer capacity (Khan, et al., 2018). This study exploits the phytochemical richness of *Prosopis cineraria* to drive the bioreduction of Fe^{3+}. This simultaneously furnished a capping layer of surface-bound phenolics, flavonoids, and carboxylate-bearing biomolecules. This strategy transformed a simple

*Author for Correspondence: Dr. K. M. Sharma, Email: kirtimohansharma@gmail.com

precipitation reaction into synthesis of structurally defined core–corona nanoarchitecture. This architecture is especially appealing, in terms of pharmaceutical-formulation considerations, with the inorganic core endowing the platform with magnetic responsiveness to site-directed drug delivery and external triggering, and the phytochemical corona providing intrinsic antioxidant payload, biocompatible surface chemistry, and anchoring sites to further conjugate therapeutic moieties (Vangijzegem et al., 2019; Mahmoudi et al., 2011).

At a mechanistic level, polyphenolic hydroxyl groups reduce Fe^{3+} via coupled single-electron transfer (SET) and hydrogen atom transfer (HAT) pathways (Lewandowska et al., 2026), with quercetin, kaempferol, gallic acid and chlorogenic acid being the primary reductants in *Prosopis cineraria* (Pandey et al., 2023; Sharma et al., 2024). Mixed-valence Fe^{2+}/Fe^{3+} hydroxides can be co-precipitated at 60 °C to yield magnetite (Fe_3O_4), and parallel oxidation of labile Fe^{2+} surface sites to form a thin passivating maghemite (γ-Fe_2O_3) shell, producing the Fe3O4/γ-Fe2O3 core/corona morphology described by Regis Correa da Silva (2024). The phytochemical layer is immobilised by catecholate and α-hydroxy-carboxylate chelation (Mohan et al., 2025) and inhibits Ostwald ripening and, most importantly, lock iron centres into redox-buffered environments that minimise uncontrolled Fenton chemistry (Ge et al., 2022).

Prosopis cineraria is a xerophytic tree that is commonly found in the dry areas of the Indian subcontinent (Gupta, 2024). It is characterized by a very broad secondary metabolite profile. Investigations have revealed that quercetin, kaempferol, rutin, gallic acid, chlorogenic acid, stachydrine, and a wide range of glucosinolates are the key bioactive compounds (Pandey et al., 2023; Sharma et al., 2024). Some of these phytochemicals themselves are known established nutraceutical antioxidant platforms with documented activity against oxidative stress-related disorders (Salehi et al., 2020; Pandey and Rizvi, 2009), which makes the species itself a particularly appealing starting material in the manufacture of pharmaceutical-grade nano-antioxidant platforms.

Although there has been an increased interest in green-synthesised iron oxide nanoparticles, there is a lack of systematic physio-chemical characterisation, coupled with multi-assay antioxidant benchmarking, of *P. cineraria*-derived materials, especially against the parent extract. The present study aimed to: (i) prepare phytochemical-capped Fe_3O_4/γ-Fe_2O_3 core-corona nanoparticles by one-pot bio-reduction of $FeCl_3$.6H2O using *P. cineraria* extract; (ii) provide systematic physicochemical characterisation (UV-Vis, FTIR, DLS, zeta potential and XRD) with explicit interpretation of features relevant to colloidal stability, surface chemistry and biocompatibility; (iii) quantify antioxidant synergy across complementary radical-scavenging assays (DPPH•, $ABTS^{\bullet+}$, and NO•) and benchmark performance against the parent extract; and (iv) discuss the translational potential of this nanoplatform to nutraceutical antioxidant formulations, magnetic drug delivery, and photo-responsive pharmaceutical applications, with explicit consideration of pro-oxidant suppression and formulation outlook.

2. MATERIALS AND METHODS

2.1 Chemicals and Reagents

Ferric chloride hexahydrate ($FeCl_3 \cdot 6H_2O$, ≥99%) was obtained from Merck. 2,2-Diphenyl-1-picrylhydrazyl (DPPH), 2,2′-azino-bis (3-ethylbenzothiazoline-6-sulphonic acid) (ABTS) and potassium persulfate were procured from Sigma-Aldrich. Griess reagent components (sulphanilamide, N-(1-naphthyl) ethylenediamine dihydrochloride and orthophosphoric acid) and sodium nitroprusside were obtained from HiMedia. All reagents were of analytical grade and used as received without further purification. Ultrapure water (18.2 MΩ·cm) was used throughout.

2.2 Plant Material and Extract Preparation

Vegetative parts of Prosopis cineraria were collected during September 2024, shade-dried at 22–25 °C and pulverised to pass through a 40-mesh sieve. An aqueous extract was prepared at a 1:10 (w/v) ratio in ultrapure water, homogenised at 10,000 rpm for 5 min, and heated at 60 °C with continuous stirring. The extract was filtered through Whatman No. 1 paper and stored at 4 °C until further use.

2.3 Green Synthesis of Iron Oxide Nanoparticles

A 100 mL aliquot of 0.1 M $FeCl_3 \cdot 6H_2O$ solution was added drop-wise (2 mL min^{-1}) into 100 mL of P. cineraria aqueous extract maintained at 60 °C under magnetic stirring (300 rpm). A characteristic colour change from yellowish-brown to black indicated the formation of FeONPs. The reaction was continued for 2 h, after which the precipitate was collected by centrifugation (10,000 rpm, 15 min), washed thrice with ultrapure water and ethanol, and freeze-dried for further characterisation.

2.4 Physicochemical Characterisation

UV-Vis absorption spectra (200–800 nm) were recorded on a Shimadzu UV-1800 spectrophotometer. FTIR analysis was performed in KBr pellet mode using a PerkinElmer Spectrum Two instrument over 4000–400 cm^{-1}. Hydrodynamic size distribution and zeta potential were measured using a Malvern Zetasizer Nano-ZS. Powder X-ray diffraction patterns were obtained with Cu Kα radiation (λ = 1.5406 Å) from 20° to 80° (2θ). The mean crystallite size (D) was calculated from the Scherrer equation, $D = K\lambda / (\beta \cos\theta)$, with K = 0.9.

2.5 Antioxidant Activity Evaluation

DPPH radical scavenging activity was determined by recording the decrease in absorbance at 517 nm following incubation of FeONPs/extract with a methanolic DPPH solution (0.1 mM) for 30 min in the dark. $ABTS^{\bullet+}$ scavenging was measured at 734 nm after reaction of test samples with a pre-formed $ABTS^{\bullet+}$ solution (ABTS + potassium persulfate, 16 h). Nitric oxide scavenging was

determined using the sodium nitroprusside–Griess method, monitoring absorbance at 546 nm. Ascorbic acid was used as the positive control in all assays. Concentration-dependent percent inhibition values were used to calculate IC_{50} by non-linear regression. All measurements were performed in triplicate.

2.6 Photocatalytic Methylene Blue Degradation

Photocatalytic activity was assessed by suspending 10 mg of FeONPs in 100 mL of 20 mg L^{-1} methylene blue (MB) solution and exposing the system to natural sunlight under continuous stirring. Aliquots were withdrawn at fixed intervals, centrifuged, and the residual MB concentration was quantified by absorbance at 664 nm. Pseudo-first-order kinetics were applied: $\ln(A_0/A_t) = k\_app \cdot t$.

2.7 Statistical Analysis

All data are expressed as mean ± standard deviation (SD; n = 3). One-way ANOVA followed by Tukey's post-hoc test was performed; $p < 0.05$ was considered statistically significant.

3. RESULTS

3.1 Characterisation of Green-Synthesised Iron Oxide Nanoparticles

3.1.1 UV-Visible Spectroscopy Analysis

UV–Vis absorption spectroscopy was used as a non-destructive primary diagnostic method, to verify the nucleation and growth of iron oxide nanoparticles using the *P. cineraria* phytochemical matrix. The absorption spectra of the purified FeONPs were found to contain four different absorption bands at 247, 380, 426, and 474 nm (Figure 1). The 247 nm high-energy band is attributed to the $Fe^{3+} \leftarrow O^{2-}$ ligand-to-metal charge-transfer (LMCT) transition of nanosized iron oxide clusters, where charge density is donated by the lattice oxide anions to the partially occupied 3d orbitals of surface Fe^{3+} centres (Abdullah et al., 2020). This extensive multiplet, spanning 380 to 474 nm, including identifiable shoulders at 426 nm is due to quantum-confinement-modulated d-d electronic transitions and interparticle plasmon coupling between the aggregated magnetite/maghemite domains in the $Fe_3O_4/\gamma\text{-}Fe_2O_3$ spinel phase. The 380–474 nm absorption bands are red-shifted compared to bulk hematite ($\alpha\text{-}Fe_2O_3$, $\lambda max \approx 400$ nm) and is expected due to the mixed-valence electronic character of the magnetite component (i.e., Fe^{2+}/Fe^{3+}) and the lack of phase-pure hematite in the product. The long-term persistence of these absorption maxima over 10 days without red-shift or expansion of the absorption bands indicates that the phytochemical corona confers long-term colloidal stability a pre-requisite to shelf-life and reproducible dosing of any nano-formulation.

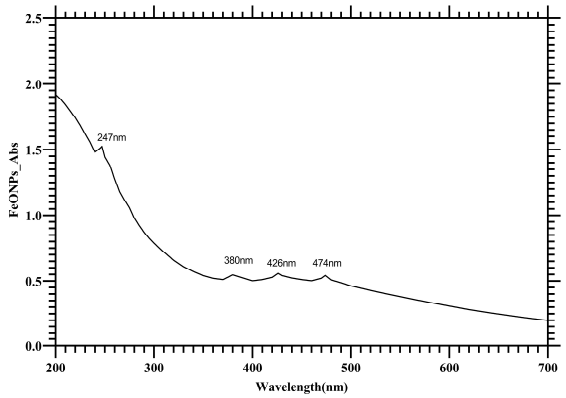

Figure 1. UV-Vis absorption spectra of P. cineraria-FeONPs. Diagnostic LMCT and plasmonic features (247, 380, 426, 474 nm) confirm the $Fe_3O_4/\gamma\text{-}Fe_2O$ spinel phase and are maintained upon storage, which is indicative of colloidal stability essential to shelf-life.

3.1.2 FTIR Spectroscopic Analysis

The functional group chemistry of the *P. cineraria*-FeONPs was characterised by FTIR spectroscopy as direct molecular evidence of the capping and surface coordination chemistry of the core–corona architecture of the phytochemicals (Figure 2). The high-intensity broad absorption at 3832–3252 cm^{-1} in the spectrum of FeONP is the combination of νO–H stretches of strongly hydrogen-bonded phenolic hydroxyl groups (as in quercetin and kaempferol catechol moieties) and νN–H stretches of proteinaceous stabilisers like stachydrine. The C═O stretching vibration was found at 1632 cm^{-1}, indicative of carboxylate–iron bidentate coordination. The chelated (bridging or bidentate) geometry of the binding is established by the complementary symmetric carboxylate stretching band at 1367 cm^{-1} (νs(COO^-)) since the splitting, $\Delta\nu = \nu as - \nu s \approx 265$ cm^{-1}, is consistent with a bidentate chelation geometry. The Fe–O lattice vibrations at 724 and 660 cm^{-1} confirm the inverse-spinel iron oxide core (Abdullah et al., 2020; Ge et al., 2022). The inferred covalent/coordinative anchoring's based on these signatures are pharmaceutically relevant as they allow the formation of stable, non-leaching phytochemical shell capable of withstanding dilution and changes in ionic strength encountered in physiological media, thereby reducing the risk of free-iron release and uncontrolled Fenton chemistry *in vivo*.

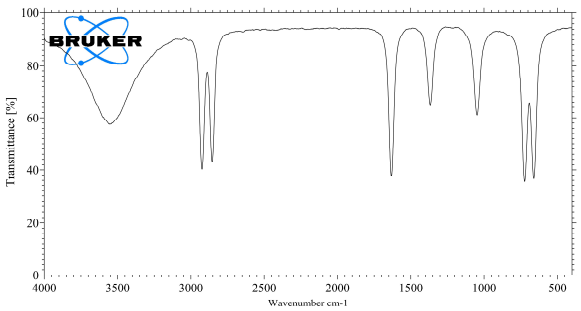

Figure 2. FTIR spectra of -FeONPs. The 3832, 3252, 1632, 1367 and 724/660 cm^{-1} bands also confirm the presence of the bidentate coordination of surface Fe centres by phenolic acids and carboxylates.

3.1.3 Particle Size Distribution and Surface Charge

DLS measurements (Figure 3A) revealed a Z-average hydrodynamic diameter of 68.5 nm and a polydispersity index (PDI) of 0.36, with a monomodal distribution centred at 68–72 nm (range 30–200 nm). Zeta potential analysis (Figure 3B) showed that there was a surface charge of −25.3 mV. Hydrodynamic dimensions of less than 100nm are favorable to cellular uptake, prolonged systemic circulation and avoidance of rapid hepatic clearance. A moderately negative zeta potential (-25.3 mV) is consistent with the use of electrosteric stabilization by the phenolic - carboxylate corona and is associated with reduced non-specific protein adsorption and lower hemolytic potential generally required in parenteral pharmaceutical formulation.

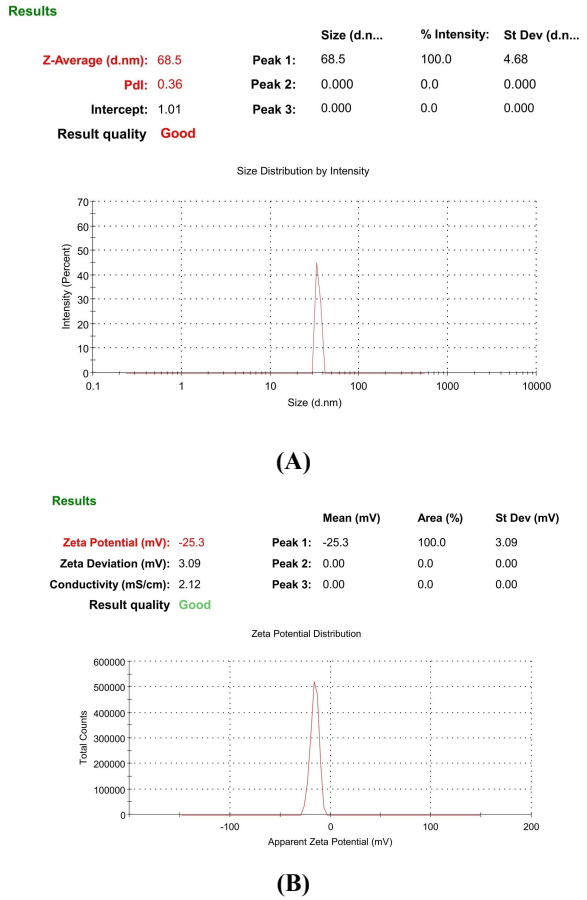

Figure 3. (A) DLS hydrodynamic size distribution and (B) zeta-potential trace of P. cineraria-FeONPs.

3.1.4 X-ray Diffraction (XRD) Analysis

Eight clearly separated Bragg reflections were observed at 2θ = 30.10°, 35.48°, 37.05°, 43.12°, 53.50°, 57.02°, 62.62° and 74.10°, indexed to the (220), (311), (222), (400), (422), (511), (440) and (533) planes of the Fe_3O_4/γ-Fe_2O_3 inverse-spinel structure (JCPDS 19-0629 / 39-1346) (Figure 4; Table 1). Mean crystallite sizes calculated via the Scherrer equation ranged from 11.4 to 14.6 nm, with an overall mean D = 12.8 ± 1.1 nm. The lack of impurities reflection (e.g. α-Fe_2O_3, FeO (OH)) and the small size distribution leads to the support of the batch-level reproducibility, an attribute that is so critical in any pharmaceutical translation.

Table 1. XRD peak parameters for *P. cineraria*-mediated FeONPs.

2θ (°)	d-spacing (Å)	Rel. Int. (%)	FWHM (°)	Miller Index	Phase	JCPDS
30.10	2.968	22	0.65	(220)	Fe_3O_4/γ-Fe_2O_3	19-0629 / 39-1346
35.48	2.529	100	0.72	(311)	Fe_3O_4/γ-Fe_2O_3	19-0629 / 39-1346
37.05	2.424	8	0.55	(222)	Fe_3O_4/γ-Fe_2O_3	19-0629 / 39-1346
43.12	2.096	38	0.68	(400)	Fe_3O_4/γ-Fe_2O_3	19-0629 / 39-1346
53.50	1.712	18	0.70	(422)	Fe_3O_4/γ-Fe_2O_3	19-0629 / 39-1346
57.02	1.614	30	0.73	(511)	Fe_3O_4/γ-Fe_2O_3	19-0629 / 39-1346
62.62	1.483	42	0.75	(440)	Fe_3O_4/γ-Fe_2O_3	19-0629 / 39-1346
74.10	1.278	12	0.78	(533)	Fe_3O_4/γ-Fe_2O_3	19-0629 / 39-1346

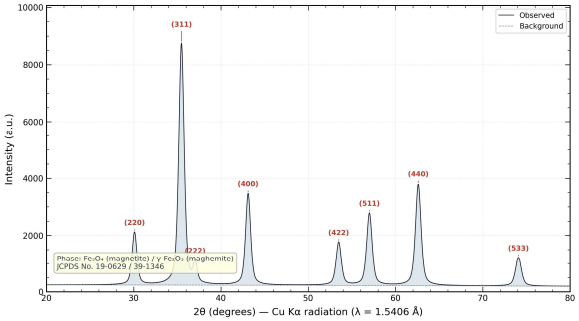

Figure 4. XRD pattern of *P. cineraria*-FeONPs indexed to the Fe_3O_4/γ-Fe_2O_3 inverse-spinel structure; phase purity and 12.8 nm crystal crystallite size support reproducible nano-formulation manufacturing

3.2 Antioxidant Activity Evaluation

3.2.1 DPPH Radical Scavenging Activity

DPPH (2,2-diphenyl-1-picrylhydrazyl) radical scavenging assay is one of the most popular, quick, and reproducible spectrophotometric techniques to assess the hydrogen atom transfer (HAT) and single-electron transfer (SET) of antioxidant substances (Gülçin and Alwasel, 2023). **Table-2** shows the percentage inhibition of DPPH by *P. cineraria* aqueous extract, *P. cineraria*-FeONPs and the positive control ascorbic acid at the concentrations of 20-100 µg/mL. The three test materials demonstrated the DPPH radical scavenging ability to increase with concentration within the range of concentrations tested (20-100 ug/mL). The *P. cineraria* extract displayed inhibition values ranging from 20.3 ± 1.3% at 20 µg/mL to 72.5 ± 2.0% at

100 µg/mL. *P. cineraria*-FeONPs always outperformed the free extract at the various concentrations, with scavenging values ranging 28.7 ± 1.4% - 83.2 ± 2.3% across the same concentration. Ascorbic acid, the standard antioxidant, showed the greatest scavenging ability in all concentrations (66.3 ± 1.5% to 98.9 ± 0.4%), as anticipated of a small-molecule electron donor with an extremely low bond-dissociation energy (BDE) of the enol C-H bond. The IC_{50} of *P. cineraria*-FeONPs (41.2 ± 1.3 ug/mL) was statistically significantly lower ($p < 0.05$, Tukey post-hoc test) than that of the free plant extract (58.9 ± 1.8 ug/mL), which was an enhancement of 1.43-fold in DPPH scavenging activity on nanoparticle formation. This super-additive response is in line with the mechanistic framework, with the nanoparticle scaffold enhancing electron-transfer capacity by improving the surface density of available Fe–O-phenolic interfaces and reducing the O-H bond

Table 2. Percent radical scavenging activity against DPPH (% inhibition ± SD, n = 3).

Concentration (µg/mL)	P. cineraria Extract	P. cineraria-FeONPs	Ascorbic Acid
20	20.3 ± 1.3	28.7 ± 1.4	66.3 ± 1.5
40	36.4 ± 1.6	49.2 ± 1.7	83.5 ± 1.2
60	50.8 ± 1.9	63.4 ± 2.1	92.1 ± 0.8
80	63.2 ± 1.8	74.6 ± 1.9	96.8 ± 0.6
100	72.5 ± 2.0	83.2 ± 2.3	98.9 ± 0.4

IC_{50} values: Extract = 58.9 ± 1.8 µg/mL; FeONPs = 41.2 ± 1.3 µg/mL; Ascorbic acid = 13.5 ± 0.7 µg/mL.

3.2.2 ABTS Radical Cation Scavenging Activity

The ABTS (2,2-azino-bis(3-ethylbenzothiazoline-6-sulfonic acid)) radical cation decolorisation assay is a complement to the DPPH assay that probes electron-transfer activity at physiologically relevant pH (7.4) and decolorises using either HAT or SET mechanisms in a highly aqueous medium, thus more accurately reflecting antioxidant efficacy in biological environments (Thongsuk and Sameenoi, 2022). *P. cineraria* extract had an ABTS scavenging inhibition of 21.6 ± 1.3% (20 µg/mL) to 74.3 ± 2.2% (100 µg/mL), whereas *P. cineraria*-FeONPs had an average better scavenging of 30.5 ± 1.5% to 84.7 ± 2.3% across the same concentration range. Ascorbic acid retained the highest overall activity (68.4 ± 1.6% to 99.1 ± 0.4%) (**Table 3)**. The IC_{50} values were 54.8 ± 2.0 µg/mL for the free extract and 40.3 ± 1.5 µg/mL for FeONPs, yielding a 1.36-fold enhancement ($p < 0.05$). The marginally lesser fold-improvement than that of the DPPH assay (1.36 vs. 1.43) might be due to the increased molecular footprint and solvation needs of the ABTS+ radical cation as compared to DPPH, which may both modulate the accessibility of radical species to the nanoparticle surface and adjust the relative contributions of the HAT and SET pathways. However, the overall high performance of FeONPs compared to the free extract in both assays is strong evidence of the structure-activity relationship that has been demonstrated to be the core-corona nanoarchitecture.

Table 3. Percent radical scavenging activity against $ABTS^{\bullet+}$ (% inhibition ± SD, n = 3).

Concentration (µg/mL)	P. cineraria Extract	P. cineraria-FeONPs	Ascorbic Acid
20	21.6 ± 1.3	30.5 ± 1.5	68.4 ± 1.6
40	38.2 ± 1.6	49.8 ± 1.7	85.9 ± 1.0
60	54.2 ± 1.9	64.3 ± 1.9	93.4 ± 0.8
80	66.3 ± 2.0	75.9 ± 2.1	97.3 ± 0.5
100	74.3 ± 2.2	84.7 ± 2.3	99.1 ± 0.4

IC_{50} values: Extract = 54.8 ± 2.0 µg/mL; FeONPs = 40.3 ± 1.5 µg/mL; Ascorbic acid = 12.6 ± 0.8 µg/mL.

3.2.3 Nitric Oxide Radical Scavenging Activity

Nitric oxide (NO•) is a key reactive nitrogen species (RNS) produced enzymatically by nitric oxide synthases and involved in physiological signaling and, in high levels, nitrosative stress and oxidative tissue damage. The Griess test, which is based on sodium nitroprusside, was used to determine the ability of test compounds to remove NO that was created in situ under aerobic conditions at physiological pH (Balkrishna et al., 2021). The *P. cineraria* extract demonstrated NO• inhibition rising from 14.8 ± 1.4% at 20 µg/mL to 69.8 ± 2.4% at 100 µg/mL. *P. cineraria*-FeONPs once again performed better than the free extract with a range of scavenging ranging between 24.3 ± 1.3% to 78.6 ± 2.2% (**Table 4)**. Ascorbic acid exhibited the highest NO• scavenging activity (58.6 ± 1.9% to 97.4 ± 0.6%), with a significantly lower IC_{50} of 21.3 ± 1.2 µg/mL. The IC_{50} values were 64.2 ± 2.4 µg/mL (extract) and 47.5 ± 1.8 µg/mL (FeONPs), representing a 1.35-fold improvement ($p < 0.05$). The general reduced NO• scavenging activity when compared to DPPH and ABTS activities (larger IC_{50} values across all samples) can be attributed to the fundamentally different radical -molecule interaction dynamics where NO 3 is a smaller, more diffusible radical compared to DPPH or $ABTS^{+\bullet}$ and its scavenging is highly sensitive to metal-chelation capacity and surface basicity, both of which are improved by the nanoparticle scaffold relative to free phenolics. The chelation of the transition metal ions which otherwise catalyze the formation of NO-derived peroxynitrite ($ONOO^-$) by the iron oxide core gives the iron oxide core an additional indirect mechanism of NO• suppression unavailable to the free plant extract.

Table 4. Percent radical scavenging activity against nitric oxide (% inhibition ± SD, n = 3).

Concentration (µg/mL)	P. cineraria Extract	P. cineraria-FeONPs	Ascorbic Acid
20	14.8 ± 1.4	24.3 ± 1.3	58.6 ± 1.9
40	27.6 ± 1.7	40.7 ± 1.6	75.8 ± 1.4
60	44.3 ± 2.1	56.8 ± 1.9	87.6 ± 1.0
80	59.4 ± 2.3	68.9 ± 2.0	94.2 ± 0.8
100	69.8 ± 2.4	78.6 ± 2.2	97.4 ± 0.6

IC_{50} values: Extract = 64.2 ± 2.4 µg/mL; FeONPs = 47.5 ± 1.8 µg/mL; Ascorbic acid = 21.3 ± 1.2 µg/mL.

3.2.4 Comparative Analysis and Synergy Assessment

A direct comparison of the IC_{50} values obtained in all the three radical-scavenging tests (**Table 5**) reveals a statistically significant decrease in the IC_{50} of *P. cineraria*-

FeONPs compared to the free plant extract in all three tests. The extent of improvement was in the rank of (DPPH) 1.43-fold, (ABTS) 1.36-fold and (NO) 1.35-fold with a synergy index of 1.35-1.43 across the three assays. The assessment of quantitative synergy was done by comparing the observed IC_{50} of the FeONPs to the hypothetical additive result based on the relative contribution of the phytochemical corona (calculated by the extract IC_{50}) and the iron oxide core (was considered insignificant alone). The IC_{50} of FeONPs would likely be similar to that of the extract under a strictly additive model, as the corona would be the major antioxidant constituent. The systematically reduced measured values of IC_{50} (synergy index = theoretical IC50/observed IC50 = 1.35-1.43) are a confirmation that the nanoparticle system is in a super-additive (synergistic) regime. The fact that three independent radical-scavenging assays converged around a 1.35-1.43-fold synergy provides strong pharmacological support that the core-corona architecture is indeed enhancing antioxidant activity instead of being a mere single-assay artefact.

Table 5. Comparative IC_{50} values (µg/mL) for in vitro antioxidant activities.

Sample	DPPH IC_{50}	ABTS IC_{50}	NO IC_{50}
P. cineraria Extract	58.9 ± 1.8[a]	54.8 ± 2.0[a]	64.2 ± 2.4[a]
P. cineraria-FeONPs	41.2 ± 1.3[b]	40.3 ± 1.5[b]	47.5 ± 1.8[b]
Ascorbic Acid (control)	13.5 ± 0.7[c]	12.6 ± 0.8[c]	21.3 ± 1.2[c]
Fold improvement	1.43	1.36	1.35

Different superscripts (a, b, c) within a column indicate statistically significant differences (Tukey's HSD, $p < 0.05$).

3.3 Photocatalytic Methylene Blue Degradation

Time-dependent UV-Vis monitoring at 664 nm (**Figure 5**) revealed a degradation efficiency of 88.2 ± 0.9% at 120 min under solar irradiation. The kinetic data fitted excellently to a pseudo-first-order model, $\ln(A_0/A_t) = k\_app \cdot t$, yielding $k\_app = 0.0177 \pm 0.0003$ min^{-1} with $R^2 = 0.9997$ and a half-life $t_{1/2} = \ln 2 / k\_app \approx 39.2$ min.

This photo-responsive behavior is pharmaceutically relevant beyond environmental remediation: it demonstrates that the same nanoplatform could be developed into a visible-light-responsive ROS generation system in photodynamic therapy or a light-responsive release system in stimuli-responsive drug delivery systems.

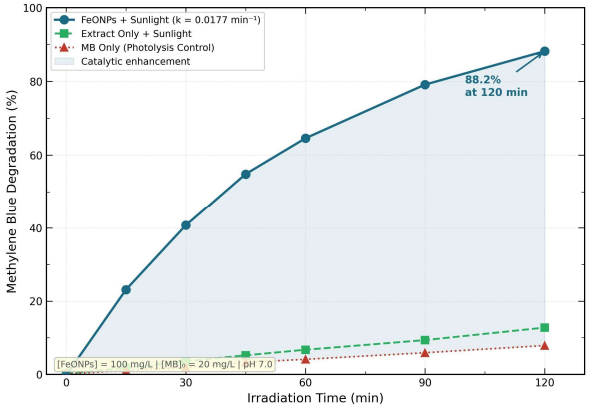

Figure 5. Time-dependent photocatalytic degradation of methylene blue (664 nm) under sunlight.

4. DISCUSSION

The complete physicochemical characterisation confirms that *P. cineraria* aqueous extract promotes the formation of a discrete, nanoscale spinel phase of $Fe_3O_4/\gamma\text{-}Fe_2O_3$ that is adorned with a chemically complex polyphenolic corona. This core/corona arrangement is the structural basis of the observed increases in both radical-scavenging and photocatalytic activity. In a pharmaceutical design, the inverse-spinel core serves as a magnetically responsive, redox-active scaffold that can be used in magnetic targeting and MRI contrast, but the multivalent phytochemical corona contains intrinsic antioxidant payload, biocompatible surface chemistry and anchoring sites of pharmaceutical conjugation. The combination of therapeutic activity and imaging/targeting ability is what constitutes a bifunctional nanoplatform, where other synthetic functionalization steps are unnecessary (Vangijzegem et al., 2019; Wu et al., 2015). The UV-Vis spectrum of the synthesised nanoparticles shows a distinct characteristic surface plasmon resonance (SPR) absorption at 247, 380, 426 and 474 nm, which can be attributed to quantum-confinement-modulated d-d electronic transitions and ligand-field transitions in the $Fe_3O_4/\gamma\text{-}Fe_2O_3$ spinel system (Abdullah et al., 2020). The 247 nm band can be ascribed to the $Fe^{3+} \leftarrow O^{2-}$ ligand to metal charge-transfer (LMCT) transition, which is typical of nanosized iron oxide clusters, and the broad features at 380–474 nm are due to interparticle plasmon coupling between aggregated magnetite/maghemite domains and are red-shifted with respect to bulk hematite (~400 nm), indicative of the mixed-valence Fe^{2+}/Fe^{3+} character of the magnetite phase. The fact that the positions of the absorption peaks remain stable over 10 days in the absence of red-shift or broadening of the band is evidence that steric stabilisation by the large phytochemical corona effectively prevents Ostwald ripening and aggregation between particles. This optical persistence is a proxy indicator of chemical-physical stability of the colloid and is directly applied to the design of long shelf-life nutraceutical or parenteral formulations.

The FTIR spectrum is direct molecular evidence of the chemical nature of the stabilising corona. The broad O–H

stretching absorption at 3832–3252 cm^{-1} presents the superposition of the hydrogen-bound phenolic hydroxyl groups (typical of quercetin, kaempferol and gallic acid) and the N–H stretches of the proteinaceous stabilisers (stachydrine). The change in the carbonyl C=O stretching frequency to 1632 cm^{-1} (instead of ~1710 cm^{-1} in free carboxylic acids) is indicative of carboxylate-iron bidentate coordination, confirming the chemisorption of gallic acid and chlorogenic acid on to Fe^{3+} surface sites via their –COOH moieties. Symmetric carboxylate stretching is supported in the surface-chelated form by the 1367 cm^{-1} band. The presence of the Fe–O lattice vibration at 724–660 cm^{-1} is an undoubted sign of the presence of an iron oxide spinel core (Abdullah et al., 2020; Ge et al., 2022). Combined, the FTIR data help validate a multi-dentate surface ligation model whereby the ortho-phenolic –OH groups and carboxylate groups of the phytochemical constituents are stable five- and six-membered chelate rings with surface Fe atoms, with the outer polysaccharide chains extended into solution to offer steric stabilisation (Thipe et al., 2019; Abdelmonem et al., 2024). This multi-dentate anchoring inhibits leaching of free iron and phenolics under physiological dilution, and reduces the risk of uncontrolled redox cycling and supporting hemocompatible behavior anticipated of a translational nano-antioxidant.

The presence of phase-pure nanocrystalline magnetite/maghemite in the sample is established by the Scherrer-derived mean crystallite size of 12.8 nm, and the lack of non-spinel reflections. The approximately 7-fold difference between crystallite size and DLS hydrodynamic diameter (68.5 nm) is a common feature of polycrystalline multi-core aggregates that are stabilised by large-molecular-weight biopolymers. In a report on FeONPs mediated by *Bauhinia variegata*, Abbas et al. (2025) measured a crystallite size of 14.3 nm versus 95 nm DLS — a similar ratio to the present system — and explained this by densely packed multi-core clusters coated by a protein-polyphenol complex. Our PDI of 0.36 is indicative of a moderately polydisperse population of particles, which is likely to happen in a single-pot synthesis of a plant-extract due to differences in local phytochemical concentration producing a distribution of nucleation times and end-product particle sizes. The multi-core morphology, which forms clustered structures, is actually beneficial to biomedical magnetism: it produces stronger collective magnetic responses to low fields than isolated single-domain particles, a property that can be exploited in magnetic drug targeting and magnetothermal stimulation (Pankhurst et al., 2009).

The statistically significant 1.43-fold reduced IC_{50} of FeONPs compared to free P. cineraria extract in the DPPH assay and the related 1.36-fold increase in ABTS scavenging, are mechanistically interpretable within the framework of surface-chemistry-enhanced electron transfer. There are four synergistic mechanisms that operate. First, enhancement in surface-to-volume ratio of the 12.8 nm nanocrystalline domain compared to bulk iron oxide enhances surface density of accessible Fe–O-phenolic interfaces by a factor of at least 3 orders of magnitude, which increases the number of redox-competent sites per unit mass proportionally. Second, the radical decolorisation between DPPH and ABTS is based on the HAT and SET; the catecholate-Fe^{3+} coordination at the surface of the nanoparticle decreases the bond-dissociation energy (BDE) of the O–H bond in the surface-chelated phenolics by depleting electron density in the oxygen atom, thus lowering the activation energy barrier to H-atom abstraction (Milenković et al., 2018). Third, H-atom donation to DPPH or ABTS produces phenoxyl radical which are promptly re-reduced by adjacent surface Fe^{2+} sites in an intramolecular electron-transfer cascade, effectively restoring the antioxidant activity of the corona and a process that is not observed in free phytochemical solution. Fourth, tight surface chelation of the iron ions with catecholate ligands inhibits the Fenton-like pro-oxidant activity ($Fe^{2+} + H_2O_2 \rightarrow \bullet OH$), which would otherwise be present in the assay media, and keeps the Fe_3O_4 core as an antioxidant scaffold instead of a pro-oxidant in the assay media (Ge et al., 2022; Liu et al., 2021). Pharmacologically, the latter point is decisive: most iron-containing nano-antioxidants have a narrow therapeutic window since the same Fe2+ centre that drives radical scavenging can also catalyze the formation of hydroxyl-radicals in vivo. It is anticipated that by locking iron centres into bidentate catecholate chelates the current core-corona system would displace the redox equilibrium to favour antioxidant chemistry rather than pro-oxidant chemistry, which is a major safety feature of any pharmaceutical-grade nano-antioxidant (Liu et al., 2021; Ge et al., 2022).

The increased NO scavenging also indicates the presence of this mechanistic model because nitric oxide radical scavenging is especially sensitive to metal-chelation ability and surface basicity; both of which are increased by the nanoparticle scaffold in comparison to free phenolics. The results are consistent with Ashrafi-Saiedlou et al. (2025), who showed that *Thymus migricus*-mediated FeONPs had a better DPPH scavenging capacity compared to the parent plant extract, which was attributed to $Fe^{2+/3+}$-mediated recovery of surface phenoxyl radicals. Abbas et al. (2025) and Abdelmonem et al. (2024) have reported similar synergy of B. variegata-FeONPs and polyphenol-magnetite hybrids, respectively, with biomedical applications. The reported 1.35-1.43-fold synergy would therefore be positioned within the upper range of reported synergy in plant systems, and the multi-radical consistency and the explicit nature based on chelation of the reported Fenton chemistry would position *P. cineraria*-FeONPs as a mechanistically defined platform instead of an empirically active formulation. The amplified radical-scavenging capacity observed in phytochemical-capped iron oxide nanoparticles relative to the free plant extract arises from at least four cooperative chemical mechanisms: (i) geometric surface-area enhancement increases the volumetric density of accessible redox-active phenolic –OH groups available for HAT and SET reactions with radical substrates (Kulhary D., 2026; Majumder et al., 2026); (ii) multivalent presentation of phenolics on the nanoparticle scaffold

reduces the enthalpic penalty of phenoxyl radical formation through cooperative delocalisation across adjacent surface-chelated molecules; (iii) the Fe^{3+}/Fe^{2+} redox couple at the nanoparticle surface catalyses electron shuttling between the phenolic corona and oxidising radical species, effectively regenerating the antioxidant capacity; and (iv) iron chelation by the surface-bound catecholate ligands suppresses Fenton-like pro-oxidant reactions ($Fe^{2+} + H_2O_2 \rightarrow Fe^{3+} + \bullet OH$) that would otherwise occur with unchelated iron centres (Ge et al., 2022; Liu et al., 2021). This mechanistic framework transforms the nanoparticle from a passive phytochemical carrier into an active catalytic antioxidant platform. It is equally important that anchoring the labile phenolics on the inorganic surface helps prevent them against autoxidation and proteolytic/esterolytic degradation pathways that limit the systemic half-life of the free polyphenols in vivo (Manach et al., 2004; Lewandrowski et al., 2026). The corona thus not only stabilizes the colloid but also stabilizes the antioxidant cargo, a feature that is very desirable in the design of orally administered nutraceutical antioxidants where bioavailability is typically the rate-limiting factor.

The observed rate constant of 0.0177 min^{-1} and 88.2% MB degradation efficiency at 120 min when using solar irradiation are a great performance of photocatalyst of a green-synthesised iron oxide catalyst. This rate is significantly higher than that of uncatalyzed photolysis (k = 0.00066 min^{-1}), which proves the dominance of heterogeneous photocatalysis by FeONP. The pseudo-first-order kinetics is consistent with the Langmuir–Hinshelwood mechanism where the surface adsorption of MB is rapid when compared to the oxidative degradation rate-limiting step. The photocatalytic process entails band-gap excitation of the Fe_3O_4/γ-Fe_2O_3 semiconductor to create e^-_CB/h^+_VB pairs; the h^+_VB oxidise surface-bound water to •OH radicals, whereas the e^-_CB reduce O_2 to $O_2\bullet^-$ and subsequently H_2O_2, completing the ROS cascade. The catecholate–Fe^{3+} LMCT transitions in the phytochemical corona provide another visible-light absorption route independent of direct semiconductor excitation to improve the harvesting of solar photons and broaden the photoactivity in the visible spectrum (Abbas et al., 2025). Photodynamic therapy (PDT) of solid tumors, antimicrobial photodynamic inactivation of resistant pathogens, and light-responsive release of payloads in photo-responsive nanocarriers are all based on the same photo-driven generation of •OH and $O_2\bullet^-$. The high quantum efficiency and visible-light activity of the current platform therefore give cause to believe that a future translational direction will be in which the same particle simultaneously scavenges extracellular ROS in physiological darkness, but is switched into an intracellular ROS-generating, cytotoxic mode upon localized visible-light exposure - an operating principle currently being actively pursued in iron-based nano-theranostics (Bouchoucha et al., 2014; Kim et al., 2017).

The current synthesis protocol is constrained by a number of chemical constraints that restrict its immediate scalability. The phytochemical analysis of *P. cineraria* also shows seasonal and geographic changes in the quercetin, kaempferol, and chlorogenic acid concentrations (Nehra et al., 2022), adding batch-to-batch variation in the rate of reduction, distribution of nanoparticle size, and corona composition. Reproducibility would be greatly enhanced by standardisation of the plant extract as a validated HPLC-based total phenolic and flavonoid determination used before nanoparticles are produced, as well as by controlled-rate addition of precursors and pH buffering. The long-term colloidal and chemical stability in physiological ionic strength and pH are yet to be determined; the comparatively moderate value of zeta potential of −25.3 mV suggests that the compression of the double-layers by the salt may stimulate the aggregation of the high-ionic-strength media. Surface PEGylation or silica encapsulation, which can be used with the green-synthesis philosophy, is a formulation strategy that should be investigated. From a regulatory/translational viewpoint, the most urgent gap is the lack of cellular cytotoxicity, hemocompatibility, and pharmacokinetic data: ICH Q3D-compliant elemental impurity profiling, MTT/lactate dehydrogenase release on physiologically relevant cell lines (HepG2, HEK-293, RBC haemolysis), genotoxicity screening, and *in vivo* biodistribution/clearance studies should be undertaken prior to any clinical positioning. Simultaneously, the systematic optimisation of corona composition, sterilization compatibility and stability under accelerated ICH will be required of pharmaceutically acceptable dosage form development enteric-coated capsules as a nutraceutical delivery system, lyophilised redispersible powders as parenteral delivery systems, and magnetic-targeted injectable suspensions. It is also suggested that the future work should consider control of the stoichiometry of Fe^{2+}:Fe^{3+} during synthesis to direct full magnetite formation and reduce the maghemite content since pure Fe_3O_4 is much more magnetically responsive in terms of magnetically recoverable catalysts. These Fe^{2+} rich variations would also be more effective in taking advantage of magnetic guidance and magnetothermal triggering in drug delivery. Together, these future-oriented considerations put *P. cineraria*-FeONPs into a convenient starting point to a green-by-design pharmaceutical nanoplatform with realistic prospects of nutraceutical, magnetic drug-delivery and photo-responsive therapeutic uses.

5. CONCLUSIONS

A structurally well-defined Fe_3O_4/γ-Fe_2O_3 core-corona nanoplatform with quercetin-, kaempferol-, gallic-acid-, and chlorogenic-acid-type phytochemicals has been obtained through a simple, one-pot, phytochemical-mediated bioreduction of $FeCl_3.6H_2O$ with *Prosopis cineraria* aqueous extract. The extensive UV-Vis, FTIR, DSL, zeta-potential and XRD characterisation defines phase-pure inverse-spinel crystallinity (D = 12.8 ± 1.1 nm), sub-100 nm hydrodynamic dimensions, and electrosterically stabilized colloidal behaviour, all of which are desirable physicochemical descriptors of pharmaceutical translation. Mechanistically, the

phytochemical corona delivers a statistically significant 1.35-1.43-fold synergistic anti-radical-scavenging IC_{50} in DPPH, ABTS and nitric oxide assays versus the parent extract that can be attributed to (i) increased surface density of redox-active phenolic-OH groups, (ii) reduced OH bond-dissociation energy through Fe^{3+}-mediated chelation, (iii) Fe^{3+}/Fe^{2+}-mediated regeneration of phenoxyl radicals, and (iv) chelation-mediated inhibition of Fenton-driven pro-oxidant chemistry. The same platform also demonstrates efficient visible-light photocatalysis (k_app = 0.0177 min^{-1}, 88.2% MB degradation in 120 min) which provides a logical basis to future photo-responsive pharmaceutical uses such as photodynamic therapy and light-triggered drug release. Combined, *P. cineraria*-FeONPs are a green-synthesized, phytochemical-capped nanoplatform with high potential in nutraceutical antioxidant formulations, magnetic drug delivery, and bifunctional theranostic applications. Future studies are needed to focus on: (i) scale-up of the extract under conditions of HPLC-standardized, GMO-compatible scale-up; (ii) systematic cytotoxicity, hemocompatibility, genotoxicity and pharmacokinetic profiling; (iii) PEGylation or silica overcoating to extend stability under conditions of physiological ionic strength; and (iv) head-to-head benchmarking against clinically approved iron oxide nanoparticles in disease models of oxidative stress. These endeavors will prove important to convert the proven antioxidant synergy into legitimate pharmaceutical action.

REFERENCES

[1] Abbas, R., Muzammil, S., Khurshid, M., & Hayat, S. (2025). Investigating the in vitro antibiofilm, antioxidant and photocatalytic potential of iron oxide nanoparticles biofabricated from Bauhinia variegata. RSC Advances, 15(54), 46009–46023.

[2] Abdelmonem, M., Albert, E. L., Alhadad, M. A., & Abdullah, C. A. (2024). Plant-polyphenol-mediated synthesis of magnetic biocompatible iron oxide nanoparticles for diagnostic imaging and management of neurodegenerative diseases. Precision Nanomedicine, 7(1), 1233–1251.

[3] Abdullah, J. A. A., Eddine, L. S., Abderrhmane, B., Alonso-González, M., Guerrero, A., & Romero, A. (2020). Green synthesis and characterization of iron oxide nanoparticles by Phoenix dactylifera leaf extract and evaluation of their antioxidant activity. Sustainable Chemistry and Pharmacy, 17, 100280.

[4] Ahmad, K. S., Yaqoob, S., & Gul, M. M. (2022). Dynamic green synthesis of iron oxide and manganese oxide nanoparticles and their cogent antimicrobial, environmental and electrical applications. Reviews in Inorganic Chemistry, 42(3), 239–263.

[5] Ajinkya, N., Yu, X., Kaithal, P., Luo, H., Somani, P., & Ramakrishna, S. (2020). Magnetic iron oxide nanoparticle (IONP) synthesis to applications: present and future. Materials, 13(20), 4644.

[6] Ali, R. (2025). Magnetically recoverable MOF-based nanocatalysts for efficient and sustainable coupling reactions. Journal of Synthetic Chemistry, 4(2), 147–165.

[7] Anselmo, A. C., & Mitragotri, S. (2019). Nanoparticles in the clinic: An update. *Bioengineering & translational medicine*, *4*(3), e10143.

[8] Ashrafi-Saiedlou, S., Rasouli-Sadaghiani, M., & Fattahi, M. (2025). Green synthesis of iron oxide nanoparticles using Thymus migricus for multifunctional applications in antioxidant, antimicrobial, photocatalytic, and seed priming processes. Heliyon, 11(5).

[9] Balkrishna, A., Kumar, A., Arya, V., Rohela, A., Verma, R., Nepovimova, E., … Kuca, K. (2021). Phytoantioxidant functionalized nanoparticles: a green approach to combat nanoparticle-induced oxidative stress. Oxidative Medicine and Cellular Longevity, 2021(1), 3155962.

[10] Bouchoucha, M., C.-Gaudreault, R., Fortin, M. A., & Kleitz, F. (2014). Mesoporous silica nanoparticles: selective surface functionalization for optimal relaxometric and drug loading performances. *Advanced Functional Materials*, *24*(37), 5911-5923.

[11] Dadfar, S. M., Roemhild, K., Drude, N. I., von Stillfried, S., Knüchel, R., Kiessling, F., & Lammers, T. (2019). Iron oxide nanoparticles: Diagnostic, therapeutic and theranostic applications. *Advanced drug delivery reviews*, *138*, 302-325.

[12] de Graft-Johnson, J. E. (2014). In vitro studies on the ferric-ion reducing ability of plant phenolics and their pro- and anti-oxidant activity in an iron-mediated hydroxyl radical oxidizing system [Doctoral dissertation, Medical University of Lodz].

[13] Ge, X., Cao, Z., & Chu, L. (2022). The antioxidant effect of the metal and metal-oxide nanoparticles. Antioxidants, 11(4), 791.

[14] Gulcin, İ., & Alwasel, S. H. (2023). DPPH radical scavenging assay. Processes, 11(8), 2248.

[15] Gupta, A. (2024). Prosopis cineraria pharmacological properties and health benefits: a review study of a potential herb of the Thar Desert. International Journal of Pharmacognosy and Life Science, 5(2B), 91–103.

[16] Khan, M., Shaik, M. R., Adil, S. F., Khan, S. T., Al-Warthan, A., Siddiqui, M. R. H., … Tremel, W. (2018). Plant extracts as green reductants for the synthesis of silver nanoparticles: lessons from chemical synthesis. Dalton Transactions, 47(35), 11988–12010.

[17] Kim, H. J., Lee, S. M., Park, K. H., Mun, C. H., Park, Y. B., & Yoo, K. H. (2015). Drug-loaded gold/iron/gold plasmonic nanoparticles for magnetic targeted chemo-photothermal treatment of rheumatoid arthritis. *Biomaterials*, *61*, 95-102.

[18] Kulhary, D., Majumder, S., Naz, E. G., Singh, Y., Pachori, S. S., Bhavsar, S. N., & Bhise, M. R. (2026). Bismuth-based organic–inorganic hybrid

perovskite $[C_{10}H_{16}N]_2BiCl_5$ as a novel visible-light active photocatalyst for the degradation of rhodamine B dye and ciprofloxacin antibiotic. Materials Science in Semiconductor Processing, 204, 110317.

[19] Lewandowska, H., Świsłocka, R., Priebe, W., Lewandowski, W., & Orzechowska, S. (2026). Towards the development of effective antioxidants — the molecular structure and properties — Part 2. Molecules, 31(4), 720.

[20] Liu, J., Ma, L., Zhang, G., Chen, Y., & Wang, Z. (2021). Recent progress of surface modified nanomaterials for scavenging reactive oxygen species in organism. Bioconjugate Chemistry, 32(11), 2269–2289.

[21] Mahmoudi, M., Sant, S., Wang, B., Laurent, S., & Sen, T. (2011). Superparamagnetic iron oxide nanoparticles (SPIONs): development, surface modification and applications in chemotherapy. *Advanced drug delivery reviews*, *63*(1-2), 24-46.

[22] Majumder, S., Karade, S. S., Kumar, R., Venkatesan, R., Alshehri, S. A., Nguyen, H. M., & Kim, K. H. (2026). Unlocking the potential of Fe_2TiO_5 nanoparticles: a promising pseudocapacitive material for next-generation supercapacitors. Materials Science in Semiconductor Processing, 202, 110194.

[23] Manach, C., Scalbert, A., Morand, C., Rémésy, C., & Jiménez, L. (2004). Polyphenols: food sources and bioavailability. *The American journal of clinical nutrition*, *79*(5), 727-747.

[24] Milenković, D., Đorović, J., Petrović, V., Avdović, E., & Marković, Z. (2018). Hydrogen atom transfer versus proton coupled electron transfer mechanism of gallic acid with different peroxy radicals. Reaction Kinetics, Mechanisms and Catalysis, 123(1), 215–230.

[25] Mohan, A., Rajendran, S., & Palani, N. (2025). Sustainable synthesis of iron oxide nanoparticles using phytochemicals: mechanisms, functionalization strategies, applications and future perspectives. Material Science and Engineering, 9(2), 36–54.

[26] Nehra, S., Gothwal, R. K., Varshney, A. K., Meena, P., Ghosh, P., & Trivedi, P. C. (2022). Bioactives and pharmacology of Capparis decidua (Forssk.) Edgew. (Syn.: Capparis aphylla Roth). In Bioactives and Pharmacology of Medicinal Plants (pp. 207–220). Apple Academic Press.

[27] Pandey, K. B., & Rizvi, S. I. (2009). Plant polyphenols as dietary antioxidants in human health and disease. *Oxidative medicine and cellular longevity*, *2*(5), 270-278.

[28] Pandey, V., Patel, S., Danai, P., Yadav, G., & Kumar, A. (2023). Phytoconstituents profiling of Prosopis cineraria and in vitro assessment of antioxidant and anti-ulcerogenicity activities. Phytomedicine Plus, 3(3), 100452.

[29] Pankhurst, Q. A., Thanh, N. T. K., Jones, S. K., & Dobson, J. (2009). Progress in applications of magnetic nanoparticles in biomedicine. *Journal of Physics D: Applied Physics*, *42*(22), 224001.

[30] Prestianni, L., Espinal, E. R., Hathcock, S. F., Vollmuth, N., Wang, P., Holler, R. A., Liu, S., Kim, B. J., & Bao, Y. (2023). Synthesis and characterization of quercetin-iron complex nanoparticles for overcoming drug resistance. Pharmaceutics, 15(4), 1041.

[31] Regis Correa da Silva, D. (2024). Unveiling the versatility of titanium and iron nanostructures: applications across medicine, environmental remediation and organic reactions [Doctoral dissertation, Université d'Ottawa/University of Ottawa].

[32] Salehi, B., Azzini, E., Zucca, P., Maria Varoni, E., V. Anil Kumar, N., Dini, L., ... & Sharifi-Rad, J. (2020). Plant-derived bioactives and oxidative stress-related disorders: a key trend towards healthy aging and longevity promotion. *Applied Sciences*, *10*(3), 947.

[33] Shah, S. T. (2022). Surface functionalization of magnetite nanoparticles with natural and multipotent antioxidants as potential nanoantioxidants and antimicrobial agents [Doctoral dissertation, University of Malaya].

[34] Sharma, V., Anand, S., Choubey, S., & Shahi, S. (2024). Prosopis cineraria: a desert treasure trove of bioactive compounds. Cuestiones de Fisioterapia, 53(03), 538–544.

[35] Thipe, V. C., Panjtan Amiri, K., Bloebaum, P., Raphael Karikachery, A., Khoobchandani, M., Katti, K. K., … Katti, K. V. (2019). Development of resveratrol-conjugated gold nanoparticles: interrelationship of increased resveratrol corona on anti-tumor efficacy against breast, pancreatic and prostate cancers. International Journal of Nanomedicine, 14, 4413–4428.

[36] Thongsuk, P., & Sameenoi, Y. (2022). Colorimetric determination of radical scavenging activity of antioxidants using Fe_3O_4 magnetic nanoparticles. Arabian Journal of Chemistry, 15(1), 103475.

[37] Vangijzegem, T., Stanicki, D., & Laurent, S. (2019). Magnetic iron oxide nanoparticles for drug delivery: applications and characteristics. *Expert opinion on drug delivery*, *16*(1), 69-78.

[38] Wu, W., Wu, Z., Yu, T., Jiang, C., & Kim, W. S. (2015). Recent progress on magnetic iron oxide nanoparticles: synthesis, surface functional strategies and biomedical applications. *Science and technology of advanced materials*, *16*(2), 023501.